ACADEMIC PRESS

Available online at www.sciencedirect.com

SCIENCE DIRECT®

Methods 30 (2003) 28–41

METHODS

www.elsevier.com/locate/ymeth

# High-resolution functional magnetic resonance imaging of the animal brain

Seong-Gi Kim[a,*] and Kamil Ugurbil[b]

[a] *Department of Neurobiology, University of Pittsburgh, 3025 East Carson Street, Pittsburgh, PA 15203, USA*
[b] *Center for Magnetic Resonance Research, University of Minnesota, Minneapolis, MN, USA*

Accepted 31 December 2002

**Abstract**

To fully understand brain function, one must look beyond the level of a single neuron. By elucidating the spatial properties of the columnar and laminar functional architectures, information regarding the neural processing in the brain can be gained. To map these fine functional structures noninvasively and repeatedly, functional magnetic resonance imaging (fMRI) can be employed. In this article the basic principles of fMRI are introduced, including specific hardware requirements and the equipment necessary for animal magnetic resonance research. Since fMRI measures a change in secondary hemodynamic responses induced by neural activity, it is critical to understand the principles and potential pitfalls of fMRI techniques. Thus, the underlying physics of conventional blood oxygenation, cerebral blood flow, and cerebral blood volume-based fMRI techniques are extensively discussed. Tissue-specific signal change is close to the site of neural activity, while signals from large vessels can be distant from the actual active site. Thus, methods to minimize large vessel contributions and to maximize tissue signals are described. The fundamental limitation of fMRI spatial resolution is the intrinsic hemodynamic response. Based on our high-resolution fMRI studies, the hemodynamic response is regulated at submillimeter functional domains and thus spatial resolution can be achieved to an order of 100 μm. Since hemodynamic responses are sluggish, it is difficult to obtain very high temporal resolution. By using an approach with multiple experiments with different stimulus conditions, temporal resolution can be improved on the order of 100 ms. With current fMRI technologies, submillimeter columnar- and laminar-specific specific functional images can be obtained from animal brains.


*Keywords:* Functional mapping; Functional magnetic resonance imaging; Blood oxygenation level dependent; Perfusion; Cerebral blood flow; Cerebral blood volume; Cortical column; Cortical lamina

## 1. Introduction

Elucidation of the temporal and spatial properties of the brain's columnar and laminar functional architectures may provide the "neural code" for information processing in the brain [1]. Visualization of such high-resolution functional localization can be achieved by 2-deoxyglucose (2-DG) autoradiography and intrinsic optical imaging. However, both approaches suffer from problems. Neither approach is nondestructive; the 2-DG method requires postmortem data collection [2], while high-resolution optical imaging requires the cortical surface to be exposed for penetration of optical light [3]. More importantly, since the penetration of light into the cortical area is limited, optical imaging cannot distinguish signals from different cortical layers on the exposed cortex, is not able to image the cortex hidden from the surface due to cortical folding, and cannot detect activity in subcortical regions. To advance our understanding of brain function, it is necessary to develop methods that can visualize the three-dimensional functional architecture of the living brain repeatedly and noninvasively. For this, functional magnetic resonance imaging (fMRI) is a good alternative (possibly the only alternative at the present), especially at the level of columnar-specific and laminar-specific high-resolution functional mapping.

The most commonly used fMRI technique relies on changes in deoxyhemoglobin (dHb) content, which acts

* Corresponding author.
*E-mail address:* kimsg@pitt.edu (S.-G. Kim).

1046-2023/03/$ - see front matter © 2003 Elsevier Science (USA). All rights reserved.
doi:10.1016/S1046-2023(03)00005-7

as an endogenous paramagnetic contrast agent [4,5]. Changes in the local dHb content in the brain lead to alterations in the signal intensity of magnetic resonance (MR) images [5–8]. It is thought that neural activation leads to an increase in oxygen delivery without a commensurate elevation in cerebral oxygen consumption [9,10], which results in a *decrease* in the capillary and venous dHb contents. Decrease in paramagnetic dHb content will enhance the magnetic resonance imaging (MRI) signal in the venous vessels as well as in the surrounding tissue. In addition blood volume changes will alter the amount of dHb (as well as oxyhemoglobin) per unit volume of brain tissue. An increase in blood volume leads to signal loss in appropriately weighted MR images. This imaging contrast is dubbed the ''blood oxygenation-level dependent'' (BOLD) contrast [5]. The BOLD imaging technique has been widely used because of its high sensitivity and easy implementation. However, since the BOLD signal is dependent on various anatomical, physiological, and imaging parameters [11], its interpretation with respect to physiological parameters is qualitative or semiquantitative. Thus, it is difficult and complicated to compare the BOLD signal changes recorded in different brain regions, to compare results from the different imaging laboratories, or even to compare results using different magnetic fields. Alternatively, cerebral blood flow (CBF) and cerebral blood volume (CBV) changes can be directly measured using MR methods. Since these fMRI signals are related to a single physiological parameter, their quantitative interpretation is considerably more straightforward.

In this article, principles and methods of various fMRI techniques are discussed. Although fMRI has been extensively used in humans, the emphasis of this article is on the application of fMRI to animal research. Since the brain size of most animals is much smaller than that of humans, it is easier to use animal research-dedicated, powerful high magnetic field scanners. We also discuss details of hardware and software requirements as well as examples of animal fMRI.

## 2. Experimental equipment and software

### 2.1. MRI hardware

To perform MRI experiments, it is necessary to have a magnetic resonance imager, which can be obtained from MRI manufacturers (such as Varian and Bruker for animal-dedicated scanners). An integrated MRI system consists of a magnet, gradient and shim coil(s) (often integrated), a console, radiofrequency (RF) and gradient amplifiers, and RF coils:

i. The most expensive item is a superconducting magnet. Strength of magnetic field ($B_0$) is defined as a unit of Tesla [1 Tesla ($=10{,}000$ gauss) is equivalent to about $20{,}000\times$ the earth's magnetic field]. Typical magnetic fields for animal research range between 4.7 T (i.e., proton resonance frequency: 200 MHz) and 11.7 T (i.e., 500 MHz), with a clear bore size 20–40 cm in diameter. It is generally accepted that for the $^1$H nucleus, signal-to-noise ratio (SNR) is linearly dependent on magnetic field strength; the higher field is in this respect the better. However, it should be noted that using a very high magnetic field requires overcoming several technical challenges such as stronger local magnetic inhomogeneities induced by tissue–air interfaces. To correct local inhomogeneous magnetic fields in the imaging volume, it is necessary to have room-temperature ''shim coils'' that generate spatially nonuniform magnetic fields that can be used to partially compensate the sample-induced nonuniformities. Higher magnetic fields require stronger shimming capability.

ii. A gradient coil set inserted into the magnet bore generates linear magnetic fields along $x$, $y$, and $z$ directions. To acquire high-resolution images at high temporal resolution, fast slew rate (i.e., switching time) and high gradient strength are necessary. Since the gradient set with a smaller coil diameter will have higher gradient strength and faster slew rate with the same electronics, it is preferable to use dedicated smaller-diameter gradients for animal research, rather than clinical gradient sets, even if clinical scanners are used. However, for a given gradient performance, the forces on the gradients increase with higher magnetic fields and consequently acoustic noise increases.

iii. The console consists of receivers that detect, amplify, demodulate, and digitize the MR signals detected by the RF coil, and a set of electronics that can generate a pattern of RF and gradient pulses (which are sent to the amplifiers) for the generation of the appropriate imaging signals from the sample. A computer controls both of these processes in the console. To obtain functional imaging, an MRI system must have high stability and high sensitivity because small differences between hundreds to thousands of images acquired during baseline (i.e. control) and stimulation periods are used to create an fMRI map. Users must pay attention to both properties. If MRI signals fluctuate 0.5% peak-to-peak over a time in a given area, it is difficult to detect a less than 0.5% signal change, which is commonly observed in fMRI.

iv. RF coils are used to transmit RF pulses for excitation of water and detect RF signals from water. Typically a smaller coil is more sensitive, but its coverage of brain area is less. For whole-brain studies, a homogenous head coil should be used, while a small surface coil can be used for localized brain studies. Although not commonly used so far in animal studies, an alternative is an ''array'' of surface coils using multiple receivers to obtain volume coverage with surface coil sensitivity, albeit at the expense of significant increase in

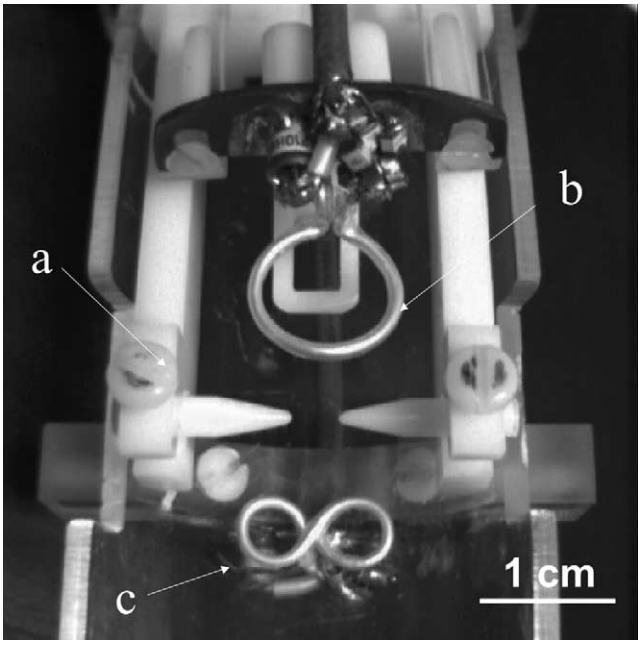


Fig. 1. Picture of a home-built rat cradle with a nonmagnetic head holder and RF coils. The nonmagnetic head holder (a) consists of two ear bars and one bite bar. The animal with the head holder is positioned inside the plastic tube, which is inserted into the magnet. In this setup, we have two coils: head coil for imaging (b) and neck coil (c) for CBF experiment. The animal's neck has to be positioned on the neck figure-8 coil for magnetically labeling water spins in the carotid arteries. The head coil is positioned on the top of head for exciting and detecting signals from the brain. In this setup, a surface coil is used for maximizing a localized brain area. To obtain entire brain images, a homogeneous coil has to be used.

instrumentation complexity and signal processing. The sensitivity of surface coil depends on depth of cortical areas, and the surface of the cortex will be most sensitive. With multiple surface coil arrays, it is in principle also possible to obtain higher sensitivity in deeper regions. In our animal studies, single surface coils were used (see Fig. 1).

### 2.2. Experimental setup of animal fMRI

Anesthetized (or awake) animals are inserted into the center of magnet bore for fMRI studies. Visual inspection of animal conditions (used in electrophysiological research) cannot be easily employed due to a long, but narrow magnet bore with all life-supporting systems. Thus, anesthetic and physiological conditions have to be carefully monitored by using remote devices outside the magnet room. Another consideration is that life-support equipment (e.g., ventilator) is located sufficiently far away from the magnet to avoid deleterious consequences of the magnetic field, resulting in difficulties in controlling the animal's physiology. To monitor animal conditions, end-tidal $CO_2$ level, body temperature, and blood pressure are continuously monitored, and blood gases are repeatedly measured.

Choice of anesthetics and level of anesthesia are important to ensure maintaining neural viability and hemodynamic response [12]. α-Chloralose is used in rat somatosensory stimulation studies [12], while isoflurane is used for cat and monkey studies [13,14]. If an anesthesia level is too high, it will suppress neural activity as well as hemodynamic response. Anesthesia level can be determined by using blood pressure, heart rate, and/or EEG activity.

To minimize potential head motions during fMRI experiments, a MRI-compatible head holder is useful. Fig. 1 shows a head holder with bite and ear bars with two MRI coils for rat studies. The nonmagnetic head holder stabilizes head position and also allows animals to be repeatedly positioned at the same location in different imaging sessions. Nonmagnetic head holders can be purchased from commercial vendors such as Kopf and Crist. For the studies reported in this article, custom-built head holders for rat and cat fMRI studies were used (see Fig. 1).

### 2.3. Basic concepts of fMRI data acquisition

Since repetitive images have to be obtained during fMRI, it is preferable to acquire images as fast as possible to improve temporal resolution and minimize motion during data acquisition. Thus, high-speed imaging approaches such as echo-planar imaging [15] and spiral imaging techniques [16] have been used. Most fMRI research sites have used the echo-planar imaging technique because of its availability and flexibility. To acquire data for an image with an $N \times M$ matrix size, a "readout" data set with $N$ points that encodes spatial information in one direction is collected $M$ times with incremental increase of the "phase-encoding" gradient that encodes spatial information in a second, orthogonal direction. Then, an image of $N \times M$ matrix size is constructed by two-dimensional Fourier transformation. With EPI images (see a review [17]), each readout data set with $N$ points is acquired repeatedly and consecutively by oscillating the readout gradients (with incremental increase in the phase-encoding gradients during each reversal) following *a single RF pulse*. Thus, the acquisition time for a single image is extremely short (approximately 15 to 100 ms). Thus, multislice images from the whole brain ("image set") can be acquired on the order of seconds. Signal fluctuations due to physiological processes can be captured accurately in time for postacquisition data processing and possible elimination.

Nominal spatial resolution of the image is determined by the "field of view" divided by matrix size. For example, a 2.0-cm field of view and 128 data points give a spatial resolution of 150 μm, provided that a postacquisition data manipulation that degenerates resolution, such as "filtering" for improved signal-to-noise ratio

(SNR), has not been performed. Actual image resolution in an EPI image is somewhat worse than the nominal resolution due to the fact that the signal is decaying during acquisition after a single RF pulse (see below). Spatial resolution is closely interrelated to temporal resolution; a higher spatial resolution requires a longer imaging time. Ignoring gradient switching time (i.e., typically 100–500 μs to reach a maximal gradient strength), the data acquisition time (AQ) for a one-shot echo-planar image (i.e., acquisition of one image after a single RF pulse) can be estimated with

$$\mathrm{AQ} = M_{\mathrm{pe}} \times N_{\mathrm{readout}} / (\gamma \times G_{\mathrm{readout}} \times FOV_{\mathrm{readout}}),$$

where $M_{\mathrm{pe}}$ is the number of phase-encoding steps, $N_{\mathrm{readout}}$ is the number of the readout data points, $\gamma$ is the gyromagnetic ratio (4258 Hz/cm/gauss for proton nuclei), $G_{\mathrm{readout}}$ is the readout gradient strength (gauss), and $FOV_{\mathrm{readout}}$ is the field of view in the readout direction (cm). For example, with the 2-cm field of view and 18-gauss readout gradient typically used in our laboratories, the acquisition time of single-shot EPI with $128 \times 128$ matrix size is approximately 107 ms without considering the gradient switching time (actually much longer than this time). It should be emphasized that data acquisition time is inversely correlated with readout gradient strength at a given spatial resolution (see MRI Hardware). During the data acquisition time, MR signals excited by a RF pulse decay by $e^{-t/T_2*}$, where $t$ is the time after the RF pulse and $T_2^*$ is the apparent transverse relaxation time (which is a reciprocal of $R_2^*$). $T_2^*$ is dependent on applied magnetic field as well as inhomogeneous local magnetic field; for example, $T_2^*$ values of gray matter water at 4.7 and 9.4 T are ~35 and ~25 ms, respectively. Thus, for high-resolution images, it is necessary to acquire multiple segments, such as four segments with each ~27 ms data acquisition time. Gaining spatial resolution results in degradation of temporal resolution. It should be noted that the MRI signal is dependent on water content in an imaging voxel. Thus, a higher spatial resolution means a lesser signal.

For fMRI studies, a larger number of image sets has to be collected during paradigms (see Fig. 2). Typically, images are acquired during repeated control and stimulation periods. Depending on stimulation paradigms, a stimulation/task duration is a subsecond to a few minutes. In our rat and cat studies, we have used a long enough stimulation duration for obtaining robust signal changes, typically a few seconds to 20 s. If a stimulation period is extremely long, the vascular response induced by the neural activity may be dampened, and a long recovery period is required.

### 2.4. Postprocessing of fMRI data

To generate a functional map from a fMRI data set, signal intensities of images obtained during control and stimulation periods are compared on a voxel-by-voxel basis (see Fig. 2). Voxels passing a statistical threshold are considered to be "active," then color-coded based on statistical values such as $t$ values. A color-coded functional map is overlaid on the anatomic image for better visualization.

fMRI data processing software can be obtained from various sources (AFNI, Brain Voyager, SPM, Stimulate, etc). Processing software contain various statistical methods as well as visualization methods. Since no gold standard exists, defining activation is not straightforward. However, common approaches use parametric statistical methods such as the $t$ test. One of the major concerns in fMRI is choice of the statistical threshold. Since a statistical value is tightly related to SNR, functional maps generated using the same statistical threshold can give different maps if SNR varies. In animal studies, signal averaging can be performed extensively. Thus, it is less likely to encounter serious problems associated with low SNR. Nevertheless, voxels deemed active because they passed a threshold are likely not the only active areas, but represent a subregion of the actual active tissue. Especially, in high-resolution images with low SNR, less active voxels may not pass a given statistical threshold. Researchers can evaluate this possibility by varying the statistical threshold. On the other hand, an active voxel may not necessarily mean that neuronal activity is present in that region, but may arise from hemodynamic signals that do not exactly colocalize with the neuronal activity (see below). Rigorous studies of fMRI signal source are essential.

Another important test is reproducibility during repeated experiments. To determine reproducibility, data sets are separated into more than one group. Although many approaches can be feasible, one simple approach is to group odd and even data acquisition groups. Then, functional maps of odd and even data sets are computed separately. Statistical values of two maps can be compared on a voxel-by-voxel basis [18]. In an ideal case with extremely high SNR, a correlation value between the two statistical maps should be close to 1.0. Also, the percentage overlap between two thresholded functional maps can be determined [19]. In the case that most voxels are active, this property is not a good indicator and its use should be avoided.

## 3. High-resolution imaging techniques

Since hemodynamic-based fMRI measures a secondary hemodynamic response induced by neural activity, it is critical to determine the relationship between neural activity and fMRI signals. To examine the correlation between BOLD responses and neural activity at a supramillimeter spatial resolution, Logothetis et al. simultaneously measured BOLD fMRI and neural

activity at the same location in the same anesthetized monkeys, and found that the BOLD signal from ~20-$mm^3$ volume is monotonically correlated with multiunit activity [20]. Similarly evoked potentials (EPs) and BOLD fMRI signals have been found to be linearly correlated even though the spatial extent of EPs is not known [21–25]. These studies indicate that the BOLD fMRI signal is well-correlated with neural activity at a coarse spatial resolution. To further examine the spatial extent of BOLD fMRI, Disbrow et al. measured BOLD fMRI with 9-$mm^3$ resolution and electrophysiolgical activity in anesthetized monkeys [22]. They found that the overlap between fMRI and electrophysiological foci was 55% and the largest mismatch between the two measurements was located at areas close to large vessels, as expected.

To obtain high-resolution fMRI, it is important to distinguish between "parenchyma" and "large vessel" components for each imaging method. The parenchyma signal is believed to be close to the site of increased neural activity [26,27]. On the other hand, functional maps based on the macrovasculature can be significantly distant from the actual site of neuronal activity [28–34]. The principal intracortical veins with average ~100-μm diameter drain from tissue volumes of 1–4 mm in diameter, and intermediate size veins (with diameter <80 μm) cover a 1-mm-diameter volume [35]. For typical human fMRI resolution such as $3 \times 3\,mm^2$, the inclusion of small vein signal does not compromise spatial specificity. However, to obtain higher-resolution functional images, signal from large vessels should be minimized.

### 3.1. Conventional BOLD approaches

It is well known that, with typical fMRI acquisition parameters, the BOLD response is particularly sensitive in and around large draining veins (see Fig. 3) because the BOLD effect is sensitive to venous blood volume and to vessel size [36,37]. To improve spatial resolution, it is important to evaluate the anatomical source of the BOLD signal and minimize large vessel contributions. The BOLD contrast induced by dHb arises from both intravascular (IV) and extravascular (EV) components. Since exchange of water between these two compartments (typical lifetime of the water in capillaries >500 ms) is relatively slow when compared with the imaging time (echo time <100 ms), MRI signals from these can be treated as separate pools.

When a blood vessel is considered as an infinite cylinder, the frequency shift $\Delta\omega$ induced by dHb within and around the vessel is depicted at Fig. 4. It should be noted that frequency ($\omega_0$) and magnetic field ($B_0$) are interchangeable because $\omega_0 = \gamma B_0$ where $\gamma$ is the gyromagnetic ratio. Inside the blood vessel, the frequency shift is expressed by

$$\Delta\omega_{in} = 2\pi\Delta\chi_0(1 - Y)\omega_0(\cos^2\theta - 1/3), \quad (1)$$

where $\Delta\chi_0$ is the maximum susceptibility difference between fully oxygenated and fully deoxygenated blood, $Y$ is the fraction of oxygenation in venous blood, $\omega_0$ is the applied magnetic field of the magnet, and $\theta$ is the angle between the applied magnetic field ($B_0$) and vessel orientation. Typically, many vessels with different orientations exist in a given voxel. When components with different frequency shifts are added within a voxel, signal loss will occur for $T_2^*$-weighted MRI. In a single large vessel, its frequency shift can be used to determine a venous oxygenation level [38].

More importantly, during fMRI measurements, water rapidly exchanges between red blood cells (RBCs) with paramagnetic dHb and plasma (average water residence time in RBCs = ~5 ms) and travel through space with inhomogeneous magnetic fields by exchange and diffusion (e.g., diffusion distance during ~50 ms measurement time = ~17 μm with diffusion constant of ~1 $\mu m^2$/ms). Thus, "dynamic" time averaging occurs over the many different fields induced by dHb. All water molecules inside the vessel will experience similar "dynamic averaging" (and will not have different phase changes within a single vessel), resulting in reduction of $T_2$ of blood water in the venous pool. It should be noted that water within vessels with different orientations will have different phases as discussed above, shortening $T_2^*$ in a given voxel. Further, at high magnetic fields, venous blood $T_2$ can be shortened relative to tissue $T_2$ because the $R_2$ ($=1/T_2$) of venous blood is quadratically dependent on magnetic field [8]. For example, $T_2$ values of tissue and venous blood are 40 and 5–7 ms at 9.4 T and 90 and 130–160 ms at 1.5 T, respectively. By setting an echo time to be much longer than $T_2^*/T_2$ of venous blood water, the IV effect can be minimized. Thus, at sufficiently high fields, venous blood signals should be virtually eliminated at echo times corresponding to tissue $T_2^*/T_2$, which was reported in the anesthetized rat somatosensory model at 9.4 T [39] and in awake human visual stimulation at 7 T [40,41]. However, most of the conventional human BOLD fMRI signals at 1.5 T originate from the IV compartment [42,43].

At any location outside the blood vessel, the frequency shift can be described by

$$\Delta\omega_{out} = 2\pi\Delta\chi_0(1 - Y)\omega_0(a/r)^2(\sin^2\theta)(\cos 2\phi), \quad (2)$$

where $a$ is the radius of the blood vessel, $r$ is the distance from the point of interest to the center of the blood vessel, and $\phi$ is the angle between $r$ and the plane defined by $B_0$ and the vessel axis. At the lumen of vessels ($r = a$), $\Delta\omega_{out}$ is identical and independent of vessel size. At $r = 5a$, the susceptibility effect is 4% of the maximally available $\Delta\omega_{out}$. The same frequency shift is observed at 15 μm around a 3-μm-radius capillary and at 150 μm around a 30-μm-radius venule (see Fig. 5). This shows

that the dephasing effect around a larger vessel is more spatially extensive because of a smaller susceptibility gradient. The EV contribution from large vessels to conventional BOLD signal is significant, regardless of magnetic field strength [39].

To minimize EV effects from large vessels, spin-echo (SE) methods can be used (e.g., [36,37,39,44,45]) for fMRI applications. The reason is that water molecules diffuse ~17 μm during a typical echo time used for fMRI studies (e.g., ~50 ms), which covers a space with the entire range of susceptibility effects around the 3-μm-radius capillary, but with a small range of static susceptibility effects around the 30-μm-radius venule. Thus, tissue water around *capillaries* will be "dynamically" averaged over the many different fields (i.e., no net phase change like the IV component). However, because tissue water around *large vessels* will be locally averaged during an echo time, the static dephasing effect is dominant (see small circles with dephasing information in Fig. 5). In a given voxel, MRI signal intensities with dephasing effects (i.e., frequency shifts) induced by numerous vessels will be summed, resulting in a decrease in $T_2^*$ and a decrease in MRI signal. The dephasing effect of the static field inhomogeneities around large vessels can be refocused by the 180° RF pulse, and no net dephasing effect will be observed. Therefore, the EV contribution of large vessels can be reduced by using the spin-echo technique (which is similar to $T_2$ weighting in diagnostic imaging). The EV and IV components of large vessels can be minimized by combining the spin-echo BOLD contrast with a long echo time at high magnetic fields (see Fig. 6). The sensitivity of spin-echo technique is two to three times less than that of gradient-echo BOLD signal even at 9.4 T [27]. Thus, at low magnetic fields, spin-echo techniques are not viable for high-resolution fMRI because of low sensitivity and contamination of the IV component [36,37,45].

Alternatively, the use of the early negative BOLD signal following the onset of stimulation has been proposed for high spatial resolution fMRI [46]. Since the source of the early negative BOLD signal is likely induced by an increase in oxygen consumption without a similar CBF response, the early negative BOLD response is indicative of metabolic change and provides a high spatial specificity [47]. This technique has been successfully applied for mapping columnar structures in anesthetized animals [13,48]. However, similar to conventional positive BOLD signal, this technique is dependent on an increase in deoxyhemoglobin in vessels and, thus, is sensitive to hemodynamic properties (e.g., vessel dimension as well as density) and biophysical properties (i.e., magnetic field and pulse sequence). This approach also requires high spatial and temporal resolution [19]. Consequently, the early negative BOLD signal has small overall contrast-to-noise ratio (small percentage changes) and is highly susceptible to physiological fluctuation and basal condition [49] (see Fig. 3).

Large vessel contributions can be also minimized by postprocessing techniques. Large draining vessels can be identified by using various BOLD signal characteristics such as a large intensity [50], a delayed response, and a significant phase change [51]. Although these subjective criteria are effective, it may not be sufficient to detect and remove all large vessel contaminations and true tissue signals cannot be separated from the EV effect induced by nearby large draining vessels. Remaining

Fig. 2 (*Top*). Schematic of functional imaging studies. Typically two-dimensional images are acquired repeatedly during control and activation periods. Data acquisition time of an image is dependent on spatial resolution and hardware capabilities. Although images can be acquired without any delay with current state-of-the-art MRI systems, it is necessary to wait to recover the signal from previous data collection. Signal-to-noise ratio (SNR), temporal resolution, and spatial resolution are interrelated. The simplest (not quite accurate) idea is that SNR × temporal resolution × spatial resolution is constant. Then, images acquired during control and stimulation periods are compared on a pixel-by-pixel basis using statistical methods such as *t* test. Only pixels passing a statistical threshold (typically $P < 0.05$) are color-coded based on statistical significance. Color-coded maps are overlaid on corresponding anatomical images.

Fig. 3 (*Middle*). Conventional gradient-echo BOLD functional study of cat brain during visual stimulation at 4.7 T [13,48]. Isoflurane was used for the entire duration of fMRI studies. Images with 64 × 64 matrix size and 2 × 2-cm field of view were obtained every 0.5 s. Data acquisition time of one image is ~50 ms. To generate a fMRI map, a cross-correlation method was used. An ideal square waveform of stimulation (e.g., consists of 0 (control) and 1 (stimulation)) was correlated with a time course on a pixel-by-pixel basis [80]. If the cross-correlation value was higher than 0.3, it was considered to be active. The fMRI signal change is localized to area 18 (left). However, the highest signal changes (indicated by yellow) are located at the sagittal sinus between the two hemispheres [48]. Bar = 1 mm. Time courses from the entire active pixels at two different physiological conditions (right). Although the same region in the same animal was used, its fMRI response is sensitive to basal physiological condition. At a higher arterial $CO_2$ level (i.e., high basal blood flow), the fMRI response is slower [49]. A similar trend was observed in awake human studies [81]. The early negative BOLD signal is also dependent on basal CBF condition. Therefore, it is important to monitor animal physiology carefully, especially for anesthetized animal studies. Typical BOLD percentage change induced by neural activity is 1–3% at 4.7 T. Bar underneath time courses = 10-s stimulation.

Fig. 4 (*Bottom left*). Diagram of a blood vessel and the parameters that determine the susceptibility effect induced by deoxyhemoglobin irons in red blood cells at a distance $r$ from the center of a vessel. The vessel with a radius of $a$ is oriented at angle $\theta$ from the main magnetic field $B_0$. $\phi$ is the angle between $r$ and plane defined by $B_0$ and the vessel axis.

Fig. 5 (*Bottom right*). Extravascular dephasing effects from a 3-μm-radius capillary and a 30-μm-radius venule. Magnitude of dephasing effect (dashed decay lines from vessels) is shown as a function of distance. Displacement of a water molecule due to diffusion is indicated. Spin-echo cannot refocus dephasing effects around a small vessel because of dynamic averaging due to diffusion, while it can refocus static dephasing (shown in averaged phases in circles).

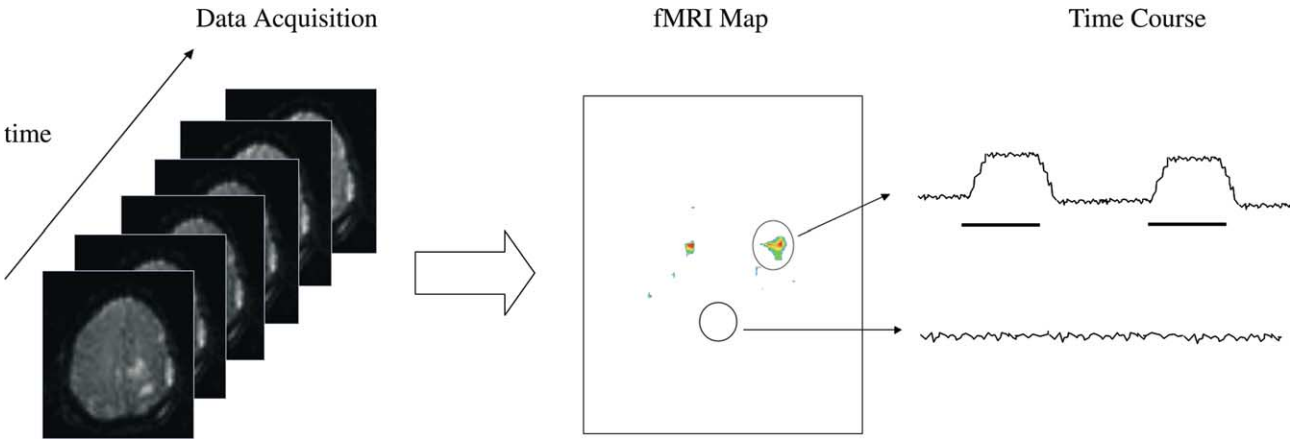


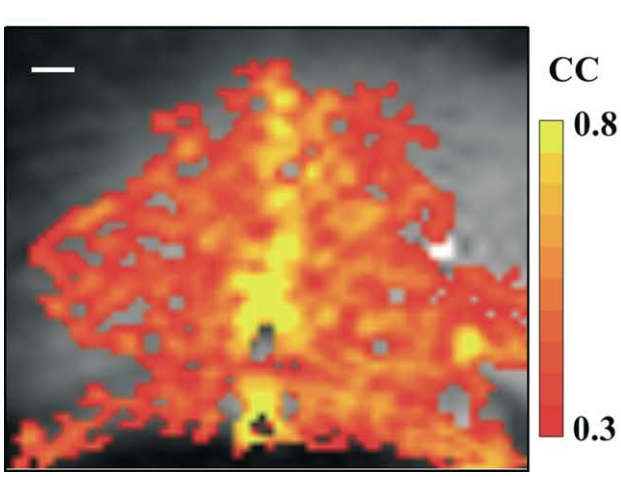


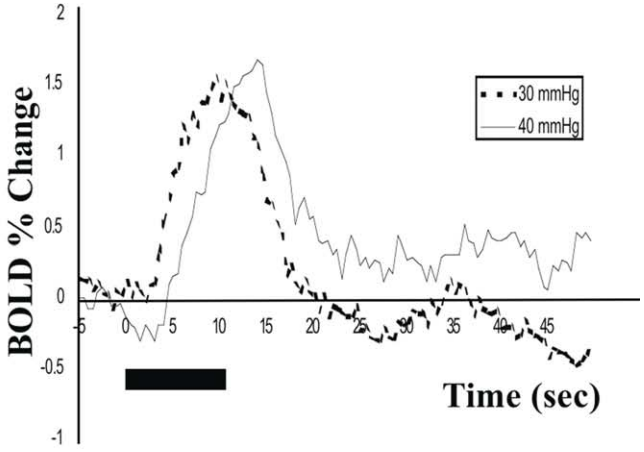


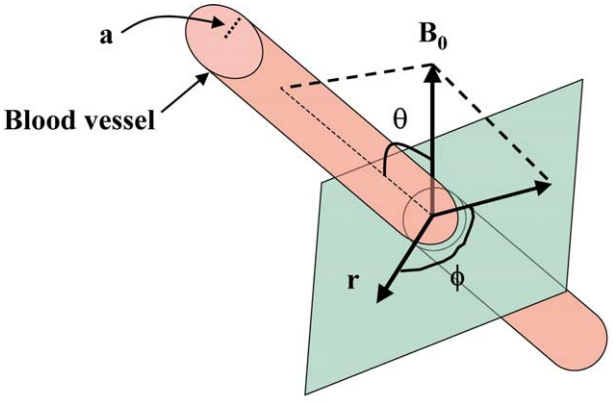


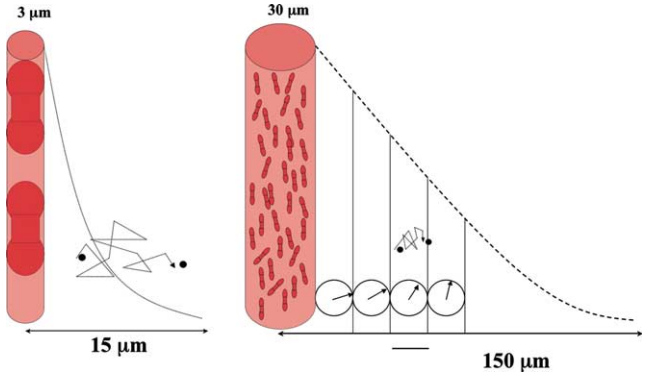


$$\Delta\omega_{in} = 2\pi\,\Delta\chi_0\,(1 - Y)\,\omega_0\,(\cos^2\theta - 1/3)$$

$$\Delta\omega_{out} = 2\pi\,\Delta\chi_0\,(1 - Y)\,\omega_0\,(a/r)^2\,(\sin^2\theta)\,(\cos 2\phi)$$

"common" large vessel contributions to the BOLD signal can be removed by the differential imaging approach for orthogonal stimuli with complementary functional territories [50,52]. However, this subtraction method cannot be used in most fMRI studies because of unknown orthogonal stimulation conditions.

### 3.2. Cerebral blood flow techniques

The above-mentioned BOLD technique is sensitive to signal changes induced by neural activity, but also sensitive to large draining vessels. Alternative techniques to the BOLD approach, which are sensitive mainly to

parenchyma, can be considered. For this, CBF measurements using $^{15}$O-labeled water as an exogenous positron emission flow tracer have been extensively performed for functional mapping, although inherent limitations on resolution due to sensitivity, positron travel distances, and detector arrangements limit the ability of this approach for high-resolution functional imaging. CBF-weighted functional images can be obtained using MR by employing arterial blood water as an endogenous flow tracer with high spatial and temporal resolution. Arterial spin labeling can be achieved by RF pulse(s). Then, labeled spins move into capillaries in the imaging slice and exchange with tissue water spins. These techniques include continuous arterial spin tagging [53], flow-sensitive alternating inversion recovery (FAIR) [54–56], and various other techniques [57–59]. In all of these techniques, two images are acquired, one with arterial spin labeling and the other without labeling. The difference in the two images is directly related to CBF (see Fig. 7), and relative CBF changes due to physiological perturbations can be measured. Most of the labeled water molecules (~90%) extract into tissue and the remaining labeled water loses most of its labeling by the time it reaches the draining veins due to its relatively short half-life (2.1 s at 9.4 T). Thus, CBF-weighted MRI signals originate predominantly from tissue/capillary in animal studies [27].

Perfusion-based fMRI techniques have been used for animal fMRI studies [19,26,27,60,61] even though wide application of perfusion imaging techniques is hampered by its poor temporal resolution of ~6 s. The spatial specificity of CBF-based fMRI is superior compared with conventional gradient echo (i.e., $T_2^*$ weighted) BOLD techniques [19,26]. In the rat somatosensory cortex, the highest CBF changes were observed in cortical layer IV, not at the surface of the cortex during somatosensory stimulation [26,27] whereas gradient echo BOLD images displayed the highest changes at the cortical surface where the large vessels are located. Layer IV specificity of the CBF response is consistent with invasive 2-DG and [$^{14}$C]iodoantipyrine autoradiographic studies in the barrel cortex [62]. The specificity of CBF response was further examined using the perfusion-based FAIR technique [54] in the cat visual areas. Fig. 8 displays a representative *t*-value map during 1-min moving gratings of single orientation [19]. Clearly, no large draining vessel contribution is present at the superior sagittal sinus which runs between the two hemispheres in this image. In contrast, the largest signal changes in conventional gradient echo BOLD fMRI in the same study were associated with the sagittal sinus. This suggests that perfusion-based fMRI signal is more specific to tissue compared with conventional BOLD contrast. More importantly, our studies show that CBF is regulated to submillimeter columnar- and laminar-specific functional domains [19,27].

### 3.3. Cerebral blood volume techniques

The CBV-based technique uses an *exogenous* intravascular contrast agents with high susceptibility. Iron oxide particles have been used as a long-half-life intravascular contrast agent [63–66], similar to endogenous irons in deoxyhemoglobin molecules (used for the BOLD contrast). Unlike in the BOLD case, however, iron oxide concentration in blood does not change with alterations in blood flow and oxygen consumption induced by neuronal activity. Thus, only when the blood volume changes, is the content of these particles in an imaging voxel perturbed. During steady state (see Fig. 9), established following the in-

Fig. 6 (*Top*). Examination of the intravascular (IV) signal contribution to spin-echo BOLD fMRI at 9.4 T [39]. An α-chloralose anesthetized rat positioned in the head holder (see Fig. 1) was used for somatosensory forelimb stimulation with repeated 1.5-mA and 3-Hz rectangular electric pulses. Left: Functional map overlaid on a coronal anatomic image. Color indicates a cross-correlation value. Localized activation is observed at the forelimb S1. Right: fMRI time courses of spin-echo BOLD signal in the primary somatosensory region. To investigate the IV component, flow-crushing gradients (in a unit of *b* value) were used. Larger *b* values result in greater reduction of the moving blood signal. If the IV component is significant, we expect a much lower BOLD signal change when a larger *b* value is used. However, we did not observe any reduction of relative BOLD signals, suggesting that spin-echo BOLD signal at 9.4 T does not contain significant IV component. Somatosensory stimulation was performed during images 20–29 (right).

Fig. 8 (*Middle*). Application of the CBF-based (FAIR) fMRI technique to isoflurane-anesthetized cat's orientation column mapping [19]. Moving gratings with black and white rectangular single-orientation bars were used for visual stimulation. The experimental condition was same as that used in Fig. 3. (A) Unlike conventional BOLD technique (see Fig. 3), CBF-weighted fMRI is specific to tissue, not draining vessels. More importantly, active clusters are irregular and column-like based on the size of clusters and the interval between clusters. Also, single-condition functional regions activated by two orthogonal orientation stimuli are complementary. Scale bar = 1 mm; color vertical bar = *t* value. (B) Time course of activation area is shown. Boxes underneath the time course indicate 1-min-long stimulation periods. Typical CBF change induced by visual stimulation ranges between 15 and 50%.

Fig. 10 (*Bottom*). Functional images of cat brain before and after injection of contrast agents [49,85]. The gradient-echo EPI technique was used for data collection. The experimental condition was the same as that used in Figs. 3a and 8. Before the injection of iron oxides, conventional positive BOLD signal change was observed at visual cortical areas. The largest (yellow color) signal change was observed at the sagittal sinus between two hemispheres and at cortical surface areas due to large vessels. After the injection of contrast agents, negative signal changes were observed, mainly in tissue area. These changes are directly related to blood volume changes. Improvement of spatial specificity using contrast agents is clearly demonstrated. Color bars = cross-correlation values.

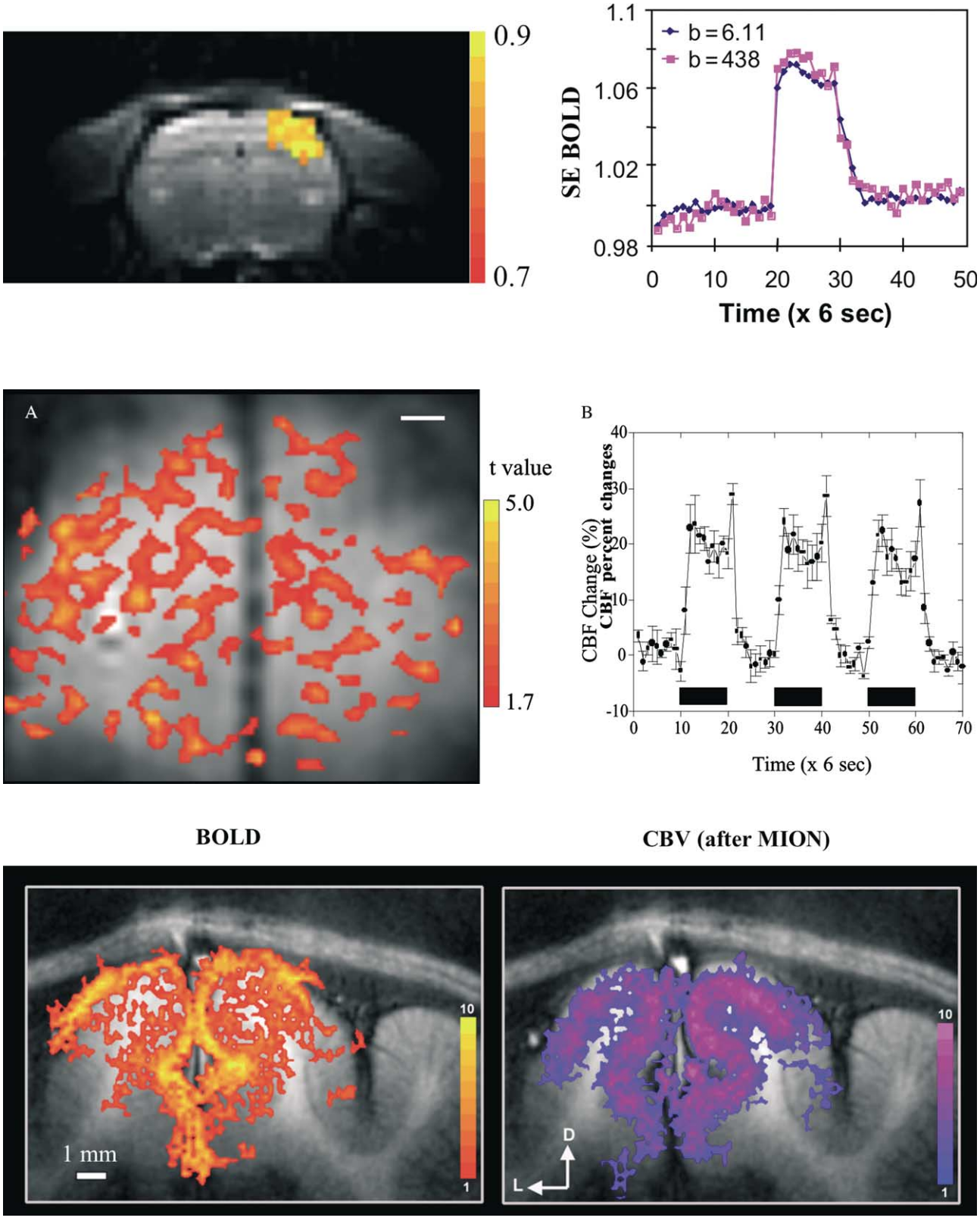


fusion of an intravascular contrast agents, an increase in CBV during stimulation will induce an increase in the content of contrast agents and, consequently, a *decrease* in MRI signal. Although the change in deoxyhemoglobin (used in the BOLD signal) will contribute to the contrast agent-enhanced MRI signal,

exogenous contrast agents in sufficiently high doses dominate the effect compared with deoxyhemoglobin. Thus, fMRI following the injection of contrast agents is weighted predominantly by the CBV change. In typical fMRI studies, neural activity induces BOLD signal increases, while CBV-weighted MRI results in signal decreases (see Fig. 10).

Since CBV is well correlated with CBF changes [67–71] and the CBF response appears to be specific to tissue, it is expected that CBV is also specific to parenchyma. Small vessels including precapillary arterioles dilate rigorously during neural stimulation, while large vessels do not dilate much [70]. Since the MRI signal is very weak in a voxel containing large vessels due to a large amount of contrast agent, its change induced by an increase in CBV may not be detected (see Fig. 9). This mechanism is similar to that of high-field BOLD for reducing the large vascular contribution. The SNR of the CBV measurement is dependent on the dose of the contrast agent, the imaging parameters, and the magnetic field. Since the BOLD contribution is supralinearly dependent on magnetic field [11] while the CBV change remains constant and iron oxides are saturated at high fields [64], SNR gain of the CBV technique over the

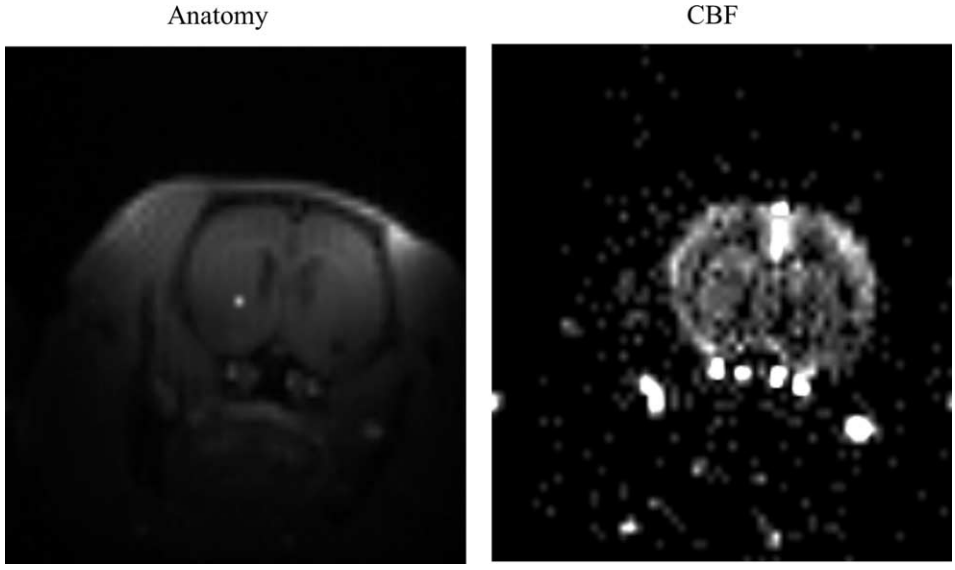


Fig. 7. Comparison between coronal anatomic and CBF images [82] of a α-chloralose-anesthetized rat. Standard inversion recovery images (the same as $T_1$ weighting in diagnostic imaging) were obtained for FAIR-based CBF measurements [54]: one with global inversion as control, the other with local inversion as flow weighting. A $T_1$-weighted anatomic image (left) was obtained as a part of FAIR measurements as a control, and a CBF image (right) was calculated by the difference between control and arterial spin labeled images. No significant signal was observed at the muscle area because of low blood flow. Although the large vessel has high signal intensity (see very bright pixels), its signal change induced by neural activity is not observed in the CBF-based fMRI measurement [19,83,84]. Signal intensity of CBF-weighted image is 1–5% of anatomic image signals.

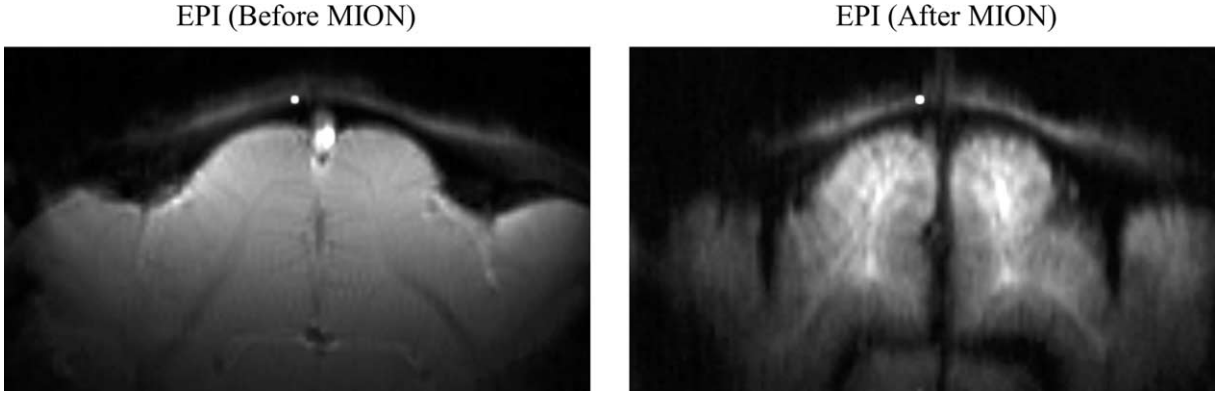


Fig. 9. High-resolution coronal images of cat brain before and after injection of contrast agents obtained at 4.7 T. Images with 150 × 150-μm in-plane resolution were obtained using the four-shot EPI technique. A solution with iron oxides (MION) of 7 mg iron/kg body wt was injected into the femoral vein as a bolus. Since contrast agents are introduced into the vascular system, significant signal loss is observed at surface vessel areas. Because of low signals at vessel areas, the cerebral blood volume-based technique is less sensitive to signal change in the large vessels.

BOLD technique is higher at low fields. Injection of large doses of contrast agents reduces $T_2^*$ of blood and surrounding tissue, and thus it is difficult to acquire high-quality images using fast imaging techniques. A typical dose is 5–10 mg iron/kg body wt. At 1.5–2 T, the improvement in sensitivity is ~5-fold [64,72], while the gain is ~1.5 to 2.0-fold at 4.7 T [64].

### 3.4. Contrast-to-noise consideration

An important consideration in fMRI is contrast-to-noise ratio, which, for fMRI, is defined as the MRI signal change due to neuronal activity relative to image-to-image signal fluctuations in consecutively acquired images. Increase in neural activity-induced MRI signal and decrease in fluctuation are important aspects for high-resolution fMRI. Neural activity-induced signal is dependent on both the magnitude of the physiological change and imaging techniques used for fMRI. In the gradient-echo BOLD- and CBV-based measurements, the signal change induced by neural activity ($\Delta S$) can be described by

$$\Delta S = \rho \cdot S_{\text{cont}} \cdot \left(e^{-\text{TE}\cdot\Delta R_2*} - 1\right), \tag{3}$$

where $\rho$ is the fraction of a voxel that is active, $S_{\text{cont}}$ is the signal intensity during the control period from the entire voxel, TE is the echo time, and $\Delta R_2^*$ is the change in the apparent transverse relaxation rate in the active partial volume. When spin-echo imaging techniques are used, $\Delta R_2^*$ is replaced by $\Delta R_2$. $\Delta R_2^*$ is equivalent to $\Delta R_2 + \Delta R_2'$ where $\Delta R_2'$ is the relaxation rate induced by local inhomogenous magnetic fields. When the spin-echo technique with an additional pulse is used, the signal loss induced by local macroscopic inhomogenous magnetic fields (on the scale of ~10 μm or larger) can be recovered. In CBF-based techniques, $\text{TE}\Delta R_2^*$ is substituted by $\text{TI}\Delta R_1^*$ where TI is the spin labeling time (i.e., the inversion time for pulsed labeling methods), and $\Delta R_1^*$ is the change in the apparent longitudinal relaxation rate. To obtain high-resolution images, $\Delta S$ should be maximized. To maximize $\Delta S$, the TE for gradient-echo studies is set to $T_2^*$ of tissue under control conditions, TE for spin-echo fMRI is set to $T_2$ of tissue, and TI for CBF is set to $T_1$ of tissue.

Sources of noise include random white noise, physiological fluctuations, bulk head motion, and system instabilities. Random noise is independent between voxels, while other noise sources may be coherent among voxels, resulting in spatial and temporal correlation. In fMRI, coherent noises are the major source of signal fluctuation except in circumstances of very high resolution where the intrinsic MR noise starts dominating. Bulk head motion can be eliminated by head holders. Physiological motion, which is due mainly to respiration and cardiac pulsation, can be minimized by gating data acquisition and/or reduced by postprocessing [73,74]. After minimizing coherent noise components, the random incoherent noise is left. It is critical that this noise does not contain contributions from instrumentation imperfections; in the highly complex MR instrument, it is easy to degrade the SNR due to less than ideal components or poor system integration. It is therefore important that the value for system "noise figure" (engineering terminology) is small. A very important factor in determining this value is the preamplifier. A typical noise figure is ~1.5 dB in a wide-band bipolar-based preamplifier used in MRI systems, and can be reduced significantly by using a narrow-band GaAs-based preamplifier.

## 4. Spatial and temporal resolution of fMRI

### 4.1. Spatial resolution

In imaging techniques that rely on secondary and tertiary responses to neuronal activity, the ultimate limit of spatial resolution is dictated by the spatial specificity of these responses. Increased neural activity induces an increase in metabolic demands. Thus, imaging the metabolic change (e.g., 2-deoxyglucose autoradiography) will yield high spatial specificity since increased metabolism will occur at the activated tissue. Changes in metabolism could modulate the hemodynamic parameters such as CBF, CBV, and venous oxygenation levels. It has been well established that the magnitude of CBF change is well correlated with that of glucose consumption change. Therefore, it may be expected the CBF and glucose consumption changes also colocalize, suggesting that CBF mapping can identify the most active regions of neural activity. This is in contrast to the most commonly used gradient-echo BOLD technique which is sensitive to paramagnetic dHb changes occurring at both the capillaries and the draining venous system; the latter reduces the spatial specificity of the conventional gradient-echo BOLD signal.

It has been suggested, based on optical imaging studies that monitor hemoglobin content (i.e., blood volume times hematocrit), and assuming that this measure also reflects CBF changes in spatial extent (due to the expected correlation between CBV and CBF), that CBF regulation is widespread beyond neuronally active areas [46]. In contrast, recent fMRI studies suggest that intrinsic CBF changes are relatively specific to submillimeter functional domains [19]. However, specificity of the hemodynamic signal is still somewhat poor compared with that of tissue metabolic signals. Among the available hemodynamic fMRI approaches, the CBF-based signal is expected to be the most specific to neuronal active sites because most of the signal originates from tissue and capillaries. CBV responses monitored by MR are expected to be somewhat less specific because

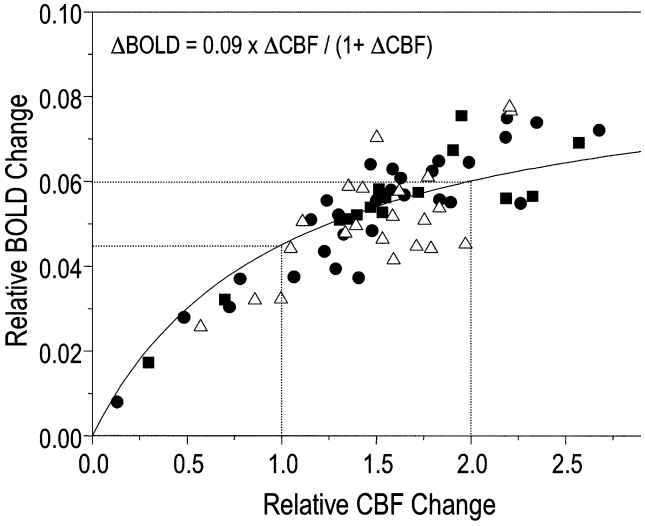


Fig. 11. Comparison of spin-echo BOLD and CBF signal changes obtained from the rat somatosensory cortex at 9.4 T [27]. Spin-echo BOLD signals obtained with spin-echo time of 40 ms do not contain large vessels (see Fig. 6). However, the relationship between BOLD and CBF is nonlinear as indicated by the best-fitted curve. Dotted lines indicate corresponding CBF and BOLD signal changes in the rat somatosensory cortex. CBF increases of 100 and 200% correspond to BOLD signals of 4.5 and 6.0%, respectively. Differential sensitivity (1.5% difference/6.0%) of the BOLD signal is much lower than that of the CBF response (100% difference/200%). A similar nonlinear relationship is expected between CBV and BOLD signals.

precapillary arterioles dilate significantly in addition to the small-diameter increase in postcapillary venules. Tissue-specific BOLD signals that can be obtained using spin-echo ($T_2$ as opposed to $T_2^*$ weighting) techniques which suppress large vessel contribution will have a spatial specificity similar to that of the CBF-weighted signal [27]. However, the relationship between CBF and BOLD signal changes is nonlinear (see Fig. 11), reducing a range of the BOLD signal change relative to that of the CBF response. Consequently, this property reduces differential sensitivity of BOLD signals obtained from cortical regions with different, but large CBF changes.

Spatial resolution of high-resolution fMRI is dependent on intrinsic hemodynamic response as well as SNR. Both factors determine the accuracy of the functional map. For the utilization of fMRI techniques, it is essential to have high SNR. Often in fMRI studies, higher-resolution functional images appear more localized because of smaller statistically significant areas. This observation should be carefully differentiated whether it originates from a lack of adequate SNR or from a genuine physiological phenomenon. Even if the source of the imaging signal is specific to neural activity, the technique that yields these signals may not be practically useful if its SNR is poor and sufficient signal averaging cannot be performed due to limited experimental time. For tissue-specific high-resolution imaging, spin-echo BOLD at very high fields and CBF and CBV methodologies can be used. Based on our experience at 4.7 and 9.4 T, the CBV technique with gradient-echo EPI data collection provides the highest contrast especially at 4.7 T. For animal fMRI studies, the CBV technique is preferable for accurate high-resolution mapping with high SNR. The CBF fMRI technique can be used because the perfusion signal is tissue-specific and extensive averaging can be performed. The spin-echo BOLD technique can be used only when ultrahigh fields (such as 9.4 T) are available.

### 4.2. Temporal resolution

Since hemodynamic responses are sluggish, it is difficult to obtain very high temporal resolution even if images can be obtained rapidly. Typically, hemodynamic signal changes are observed 1–2 s after onset of neural stimulation and reach a maximum at 5–8 s (see Fig. 3). The exact time of neural activity from hemodynamic responses cannot be easily obtained. The important question is to determine sequential neural activities of different cortical regions. If the hemodynamic response times in all regions and in all subjects were the same, neuronal activities could be directly inferred from fMRI time courses. However, since the hemodynamic response is closely related to the vascular architecture, this may not be true in all regions and in all subjects, and thus differences in fMRI time courses may be simply related to intrinsic hemodynamic response time differences, hampering temporal studies. Thus, temporal resolution of fMRI is limited. Alternative approaches to overcome these problems have been proposed. To separate intrinsic hemodynamic differences from neural activity differences, a time-resolved event-related fMRI technique can be used [75–78]. The idea is to examine how fMRI parameters vary with behavioral correlates; thus, the approach requires multiple behavioral outcome measures. Subsequently, temporal characteristics of fMRI responses can be correlated with behavioral data such as response time. Differences in the underlying temporal behavior of neuronal activity can be distinguished from hemodynamic response time variations between subjects and brain areas (see review article [79]). This approach allows the experimenter to obtain higher temporal resolution. Dynamic fMRI studies can be feasible using standard gradient-echo BOLD and CBV-weighted fMRI. To obtain high spatial and temporal resolution, the CBV-weighted fMRI technique is most appropriate for animal studies.

## 5. Conclusions

Advancement of imaging technologies allows the detection of various vascular physiological parameters

induced by neural activity. Fortunately, tissue-based hemodynamic response is specific to neuronal active sites at the level of cortical column and lamina. Thus, the spatial resolution achieved by fMRI can be on the order of 100 μm in animals, allowing mapping of column- and layer-specific neural activities. Since hemodynamic response is slow, its temporal resolution cannot be reached at a level of neural activity time scale easily. By using an approach with multiple experiments with different stimulus intervals or durations, temporal resolution can be improved up to on the order of 100 ms. The methodological developments that have made such measurements possible have taken place in a short period, demonstrating the flexibility of the MR approach. It is therefore not inconceivable that significant further achievements using MR methodology will be realized through research in MR physics.

## Acknowledgments

This work is supported by the National Institutes of Health (NS38295, NS40719, and NS44589), the McKnight Foundation, and the Keck Foundation.

## References

[1] D. Hubel, T. Wiesel, J. Physiol. London 160 (1962) 106–154.
[2] L. Sokoloff, M. Reivich, C. Kennedy, M. Des Rosiers, G. Patlak, K. Pettigrew, O. Sakurada, M. Shinohara, J. Neurochem. 28 (1977) 897–916.
[3] A. Grinvald, E. Leike, R.D. Frostig, C.D. Gillbert, T.N. Wiesel, Nature 324 (1986) 361–364.
[4] L. Pauling, C.D. Coryell, Proc. Natl. Acad. Sci. USA 22 (1936) 210–216.
[5] S. Ogawa, T.-M. Lee, A.S. Nayak, P. Glynn, Magn. Reson. Med. 14 (1990) 68–78.
[6] S. Ogawa, T.-M. Lee, A.R. Kay, D.W. Tank, Proc. Natl. Acad. Sci. USA 87 (1990) 9868–9872.
[7] S. Ogawa, T.M. Lee, Magn. Reson. Med. 16 (1990) 9–18.
[8] K.R. Thulborn, J.C. Waterton, P.M. Mattews, G.K. Radda, Biochim. Biophys. Acta 714 (1982) 265–270.
[9] P.T. Fox, M.E. Raichle, M.A. Mintun, C. Dence, Science 241 (1988) 462–464.
[10] P.T. Fox, M.E. Raichle, Proc. Natl. Acad. Sci. USA 83 (1986) 1140–1144.
[11] S. Ogawa, R.S. Menon, S.-G. Kim, K. Ugurbil, Annu. Rev. Biophys. Biomol. Struct. 27 (1998) 447–474.
[12] M. Ueki, G. Miles, K.-A. Hossmann, Acta Anaesthesiol. Scand. 36 (1992) 318–322.
[13] D.-S. Kim, T.Q. Duong, S.-G. Kim, Nat. Neurosci. 3 (2000) 164–169.
[14] N.K. Logothetis, H. Guggenberger, S. Peled, J. Pauls, Nat. Neuroscience 2 (1999) 555–562.
[15] P. Mansfield, J. Phys. C 10 (1977) L55–L58.
[16] C. Ahn, J.H. Kim, Z.H. Cho, IEEE Trans. Med. Imaging MI-5 (1986) 2–7.
[17] M. Stehling, R. Turner, P. Mansfield, Science 254 (1991) 43–50.
[18] C. Tegeler, S.C. Strother, J.R. Anderson, S.-G. Kim, Hum. Brain Mapp. 7 (1999) 267–283.
[19] T.Q. Duong, D.-S. Kim, K. Ugurbil, S.-G. Kim, Proc. Natl. Acad. Sci. USA 98 (2001) 10904–10909.
[20] N.K. Logothetis, J. Pauls, M. Augath, T. Trinath, A. Oeltermann, Nature 412 (2001) 150–157.
[21] G. Brinker, C. Bock, E. Busch, H. Krep, K.-A. Hossman, M. Hoehn-Berlage, Magn. Reson. Med. 41 (1999) 469–473.
[22] E.A. Disbrow, D.A. Slutsky, T.P.L. Roberts, L.A. Krubitzer, Proc. Natl. Acad. Sci. USA 97 (2000) 9718–9723.
[23] S. Ogawa, T.-M. Lee, R. Stepnoski, W. Chen, X.-H. Zhu, K. Ugurbil, Proc. Natl. Acad. Sci. USA 97 (2000) 11026–11031.
[24] O.J. Arthurs, E.J. Williams, T.A. Carpenter, J.D. Pickard, S.J. Boniface, Neuroscience 101 (2000) 803–806.
[25] K. Kashikura, J. Kershaw, S. Yamamoto, X. Zhang, T. Matsuura, I. Kanno, Magn. Reson. Med. 45 (2001) 212–216.
[26] T.Q. Duong, A.C. Silva, S.-P. Lee, S.-G. Kim, Magn. Reson. Med. 43 (2000) 383–392.
[27] S.-P. Lee, A.C. Silva, S.-G. Kim, Magn. Reson. Med. 47 (2002) 736–741.
[28] S. Lai, A.L. Hopkins, E.M. Haacke, D. Li, B.A. Wasserman, P. Buckley, H. Friedman, H. Meltzer, H. Hedera, R. Friedland, Magn. Reson. Med. 30 (1993) 387–392.
[29] R.S. Menon, S. Ogawa, D.W. Tank, K. Ugurbil, Magn. Reson. Med. 30 (1993) 380–386.
[30] S.-G. Kim, K. Hendrich, X. Hu, H. Merkle, K. Ugurbil, NMR Biomed. 7 (1/2) (1994) 69–74.
[31] J. Frahm, K.-D. Merboldt, W. Hanicke, A. Kleinschmidt, H. Boecker, NMR Biomed. 7 (1/2) (1994) 45–53.
[32] C. Segebarth, V. Belle, C. Delon, R. Massarelli, J. Decety, J.-F. Le Bas, M. Decorpts, A.L. Benabid, Neuroreport 5 (1994) 813–816.
[33] S.-G. Kim, K. Ugurbil, J. Neurosci. Methods 74 (1997) 229–243.
[34] K. Ugurbil, X. Hu, W. Chen, X.H. Zhu, S.-G. Kim, A. Georgopoulos, Phil. Trans. R. Soc. London B 354 (1999) 1195–1213.
[35] H. Duvernoy, S. Delon, J. Vannson, Brain Res. Brain 7 (1981) 519–579.
[36] S. Ogawa, R.S. Menon, D.W. Tank, S.-G. Kim, H. Merkle, J.M. Ellermann, K. Ugurbil, Biophys. J. 64 (1993) 800–812.
[37] R.M. Weisskoff, C.S. Zuo, J.L. Boxerman, B.R. Rosen, Magn. Reson. Med. 31 (1994) 601–610.
[38] F.G.C. Hoogenraad, J.R. Reichenbach, E.M. Haacke, S. Lai, K. Kuppusamy, M. Sprenger, Magn. Reson. Med. 389 (1998) 97–107.
[39] S.-P. Lee, A.C. Silva, K. Ugurbil, S.-G. Kim, Magn. Reson. Med. 42 (1999) 919–928.
[40] E. Yacoub, A. Shmuel, J. Pfeuffer, P. Van De Moortele, G. Adriany, P. Andersen, J. Vaughan, H. Merkle, K. Ugurbil, X. Hu, Magn. Reson. Med. 45 (2001) 588–594.
[41] T.Q. Duong, E. Yacoub, G. Adriany, X. Hu, K. Ugurbil, S.-G. Kim, Magn. Reson. Med. (2003) in press.
[42] A.W. Song, E.C. Wong, S.G. Tan, J.S. Hyde, Magn. Reson. Med. 35 (1996) 155–158.
[43] J. Zhong, R.P. Kennan, R.K. Fulbright, J.C. Gore, Magn. Reson. Med. 40 (4) (1998) 526–536.
[44] P.A. Bandettini, E.C. Wong, A. Jesmanowicz, R.S. Hinks, J.S. Hyde, NMR Biomed. 7 (1994) 12–20.
[45] J. Oja, J. Gillen, R. Kauppinen, M. Kraut, P. van Zijl, Magn. Reson. Med. 42 (1999) 617–626.
[46] D. Malonek, A. Grinvald, Science 272 (1996) 551–554.
[47] I. Vanzetta, A. Grinvald, Science 286 (1999) 1555–1558.
[48] T.Q. Duong, D.-S. Kim, K. Ugurbil, S.-G. Kim, Magn. Reson. Med. 44 (2000) 231–242.
[49] N. Harel, S.-P. Lee, T. Nagaoka, D.-S. Kim, S.-G. Kim, J. Cereb. Blood Flow Metab. 22 (2002) 908–917.
[50] K. Cheng, R. Waggoner, K. Tanaka, Neuron 32 (2001) 359–374.
[51] R.S. Menon, Magn. Reson. Med. 47 (2002) 1–9.
[52] B. Goodyear, R.S. Menon, Hum. Brain Mapp. 14 (2001) 210–217.

[53] J.A. Detre, J.S. Leigh, D.S. Williams, A.P. Koretsky, Magn. Reson. Med. 23 (1992) 37–45.
[54] S.-G. Kim, Magn. Reson. Med. 34 (1995) 293–301.
[55] K.K. Kwong, D.A. Chesler, R.M. Weisskoff, K.M. Donahue, T.L. Davis, L. Ostergaard, T.A. Campbell, B.R. Rosen, Magn. Reson. Med. 34 (1995) 878–887.
[56] C. Schwarzbauer, S. Morrissey, A. Haase, Magn. Reson. Med. 35 (1996) 540–546.
[57] R.R. Edelman, B. Siewert, D.G. Darby, V. Thangaraj, A.C. Nobre, M.M. Mesulam, S. Warach, Radiology 192 (1994) 513–520.
[58] J. Helpern, C. Branch, M. Yongbi, N. Huong, Magn. Reson. Imaging 15 (1997) 135–139.
[59] E. Wong, R. Buxton, L. Frank, Magn. Reson. Med. 39 (1998) 702–708.
[60] A. Silva, S.-P. Lee, C. Yang, C. Iadecola, S.-G. Kim, J. Cereb. Blood Flow Metab. 19 (1999) 871–879.
[61] A.C. Silva, S.-P. Lee, C. Iadecola, S.-G. Kim, J. Cereb. Blood Flow Metab. 20 (2000) 201–206.
[62] T.A. Woolsey, C.M. Rovainen, S.B. Cox, M.H. Henegar, G.E. Liang, D. Liu, Y.E. Moskalenko, J. Sui, L. Wei, Cereb. Cortex 6 (1996) 647–660.
[63] R.P. Kennan, B.E. Scanley, R.B. Innis, J.C. Gore, Magn. Reson. Med. 40 (1998) 840–846.
[64] J.B. Mandeville, J.J. Marota, B.E. Kosofsky, J.R. Keltner, R. Weissleder, B.R. Rosen, Magn. Reson. Med. 39 (1998) 615–624.
[65] N. van Bruggen, E. Busch, J.T. Palmer, S.-P. Williams, A.J. de Crespigny, J. Cereb. Blood Flow Metab. 18 (1998) 1178–1183.
[66] J.B. Mandeville, B.G. Jenkins, B.E. Kosofsky, M.A. Moskowitz, B.R. Rosen, J.J.A. Marota, Magn. Reson. Med. 45 (2001) 443–447.
[67] R.L. Grubb, M.E. Raichle, J.O. Eichling, M.M. Ter-Pogossian, Stroke 5 (1974) 630–639.
[68] M. Jones, J. Berwick, D. Johnston, J. Mayhew, Neuroimage 13 (2001) 1002–1015.
[69] H. Ito, K. Takahashi, J. Hatazawa, S.-G. Kim, I. Kanno, J. Cereb. Blood Flow Metab. 21 (2001) 608–612.
[70] S.-P. Lee, T. Duong, G. Yang, C. Iadecola, S.-G. Kim, Magn. Reson. Med. 45 (2001) 791–800.
[71] M. Jones, J. Berwick, J. Mayhew, Neuroimage 15 (2002) 474–487.
[72] W. Vanduffel, D. Fize, J.B. Mandeville, K. Nelissen, P. van Hecke, B.R. Rosen, R.B.H. Tootell, G.A. Orban, Neuron 32 (2001) 565–577.
[73] X. Hu, S.-G. Kim, Magn. Reson. Med. 31 (1994) 495–503.
[74] X. Hu, T.H. Le, T. Parrish, P. Erhard, Magn. Reson. Med. 34 (1995) 210–221.
[75] S.-G. Kim, W. Richter, K. Ugurbil, Magn. Reson. Med. 37 (1997) 631–636.
[76] W. Richter, P.M. Andersen, A.P. Georgopoulos, S.-G. Kim, Neuroreport 8 (1997) 1257–1261.
[77] W. Richter, K. Ugurbil, A.P. Georgopoulos, S.-G. Kim, Neuroreport 8 (1997) 3697–3702.
[78] W. Richter, R. Somorijai, R. Summers, M. Jarmasz, R.S. Menon, J.S. Gati, A.P. Georgopoulos, C. Tegeler, K. Ugurbil, S.-G. Kim, J. Cogn. Neurosci. 12 (2000) 310–320.
[79] R. Menon, S.-G. Kim, Trends Cogn. Sci. 3 (1999) 207–215.
[80] P.A. Bandettini, A. Jesmanowicz, E.C. Wong, J.S. Hyde, Magn. Reson. Med. 30 (1993) 161–173.
[81] E.R. Cohen, K. Ugurbil, S.-G. Kim, J. Cereb. Blood Flow Metab. 22 (2002) 1042–1053.
[82] N.V. Tsekos, F. Zhang, H. Merkle, M. Nagayama, C. Iadecola, S.-G. Kim, Magn. Reson. Med. 39 (1998) 564–573.
[83] S.-G. Kim, N.V. Tsekos, Magn. Reson. Med. 37 (1997) 425–435.
[84] S.-G. Kim, N.V. Tsekos, J. Ashe, NMR Biomed. 10 (1997) 191–196.
[85] S.-G. Kim, S. Ogawa, Curr. Opin. Neurobiol. 12 (2002) 607–615.